Differential inhibition of pyramidal cells and inhibitory interneurons along the rostrocaudal axis of anterior piriform cortex

Adam M. Large[a], Nathan W. Vogler[a,1], Martha Canto-Bustos[a,1], F. Kathryn Friason[a], Paul Schick[a], and Anne-Marie M. Oswald[a,2]

[a]Department of Neuroscience, Center for the Neural Basis of Cognition, University of Pittsburgh, Pittsburgh, PA 15213

The spatial representation of stimuli in sensory neocortices provides a scaffold for elucidating circuit mechanisms underlying sensory processing. However, the anterior piriform cortex (APC) lacks topology for odor identity as well as afferent and intracortical excitation. Consequently, olfactory processing is considered homogenous along the APC rostral–caudal (RC) axis. We recorded excitatory and inhibitory neurons in APC while optogenetically activating GABAergic interneurons along the RC axis. In contrast to excitation, we find opposing, spatially asymmetric inhibition onto pyramidal cells (PCs) and interneurons. PCs are strongly inhibited by caudal stimulation sites, whereas interneurons are strongly inhibited by rostral sites. At least two mechanisms underlie spatial asymmetries. Enhanced caudal inhibition of PCs is due to increased synaptic strength, whereas rostrally biased inhibition of interneurons is mediated by increased somatostatin–interneuron density. Altogether, we show differences in rostral and caudal inhibitory circuits in APC that may underlie spatial variation in odor processing along the RC axis.

olfactory | cortex | inhibitory circuits

It is well-established that the spatial organization of sensory information plays an important role in neocortical sensory processing. The retinotopic, tonotopic, and somatotopic maps established at the periphery form the basis of stimulus representation in primary visual, auditory, and somatosensory cortices. This spatial organization is perhaps the oldest and best understood feature of sensory codes.

In the olfactory system, odor components are encoded by individual olfactory receptor neurons (ORNs) that express a single receptor gene. All ORNs expressing the same receptor project axons to approximately two target glomeruli in the olfactory bulb (OB) (1, 2). Within the OB, individual mitral/tufted (M/T) cells extend apical dendrites to a single glomerulus (3) and respond selectively to glomerular activation (4, 5). This exquisite connection specificity produces a discrete spatial organization of odor information within the OB (6–9). However, just one synapse away in the anterior piriform cortex (APC), any semblance of spatial representation for odor identity is lost (10–12).

The piriform cortex is a trilaminar cortex that extends along the rostral–caudal (RC) axis of the ventral rodent brain. The two main subdivisions, APC and posterior piriform cortex (PPC), differ with respect to afferent and efferent projections (13–15) as well as functional roles in olfactory processing (16–19). However, despite the fact that each region comprises ~1–2 mm of the RC axis, odor processing within APC or PPC is considered spatially homogenous. The APC is delineated by the lateral olfactory tract (LOT) that delivers odor information directly from the OB. Single M/T cell axons branch extensively along the entirety of the LOT (20–22), resulting in a diffuse pattern of afferent excitation. Likewise, recurrent connections between principal neurons within APC extend over millimeter distances without decrement (23, 24). Consistent with this excitatory architecture, there is no

topography for odor identity in APC. Neurons responsive to a single odor are distributed on the RC axis of the APC (10, 11, 25), and nearby neurons respond to different odors (11, 12, 26, 27). The absence of an "odortopic" map suggests that, unlike sensory neocortex, space is not a dimension for odor coding in APC.

Given the seemingly uniform distributions of excitation and odor responses, a surprising finding is that intracortical inhibition is not spatially uniform along the RC axis (28). Specifically, pyramidal cells (PCs) receive stronger inhibition from caudal stimulation sites than rostral sites. In medial entorhinal cortex, similar inhibitory asymmetry exists that is mediated by parvalbumin (PV) interneurons and supports dorsoventral patterning of gamma-band oscillatory frequencies (29). However, the circuit mechanisms and the potential role of asymmetric inhibition in APC are unknown.

In this study, we use optogenetic tools (30) to investigate the spatial patterning of inhibition onto excitatory semilunar (SL) cells and PCs in L2 and PCs in L3 as well as L1–L3 inhibitory interneurons. We find that spatial asymmetries in inhibition are primarily a property of recurrent circuits in L3 of APC as opposed to superficial layers that comprise afferent circuits. A striking finding is that spatial asymmetries in L3 are in opposition. PCs receive stronger inhibition from caudal locations, while

Significance

In most primary sensory cortical areas, sensory information is topographically organized. The spatial mapping of sensory features has proven useful in elucidating circuit mechanisms that underlie sensory representations in the brain. The piriform cortex is postulated to play a prominent role in the formation of odor percepts but lacks a topographic representation for odor information. Consequently, the circuit mechanisms underlying odor processing have remained elusive. We show spatial patterning of inhibition along the rostrocaudal axis of piriform cortex that differs with respect to excitatory and inhibitory neurons. Exploration of the underlying mechanisms revealed that inhibitory circuits differ in rostral vs. caudal piriform cortex. This rostrocaudal spatial organization could provide a scaffold for investigating circuit computations during odor processing.

L3 interneurons receive greater inhibition from rostral locations. The mechanisms underlying inhibitory asymmetries differ between L3 PCs and interneurons. Analysis of spontaneous inhibitory postsynaptic currents (sIPSCs) in PCs revealed that sIPSC strength, but not the frequency, increases along the RC axis. Furthermore, spontaneous excitatory postsynaptic current (sEPSC) and sIPSC amplitudes are correlated in caudal but not rostral PCs. This suggests that postsynaptic plasticity underlies stronger caudal inhibition of PCs. However, rostrally biased inhibition of interneurons is mediated by somatostatin (SST) interneurons that decrease in density along the RC axis. Altogether, these findings show that neural circuits differ in rostral vs. caudal APC and challenge the notion that olfactory processing is spatially homogeneous in APC.

Results

PCs Receive Stronger Inhibition from Caudal APC. Spatially asymmetric inhibition of PCs in APC (28) has been previously shown using glutamate uncaging. Specifically, PCs receive stronger inhibition from caudal uncaging sites. However, the mechanisms underlying asymmetric inhibition are unknown. Since uncaging methods could activate both excitatory and inhibitory neurons, we investigated whether inhibitory circuits alone are sufficient to reproduce inhibitory asymmetries. We selectively activated interneurons that express Channelrhodopsin (ChR2) under the promoter for vesicular GABA transporter (VGAT) using restricted blue light spots (~70-μm diameter) in a 4 × 5 grid surrounding the recorded cell [schematic in Fig. 1*A1* (31)]. We stimulated each grid site with two brief light pulses (100-ms interpulse interval), but only the IPSC in response to the first pulse was analyzed (*Methods*). We recorded SL cells and superficial PCs in L2 as well as deep PCs in L3. Recorded neurons were centrally located along the RC axis in sagittal slices of APC. The inhibitory strength at each location was quantified as the area (picoamperes · seconds) under average IPSC (Fig. 1 *B1*, *C1*, and *D1*). We have previously reported that inhibitory strength varies by cell type and layer (31). Specifically, L3 interneurons provide the strongest inhibition, while L3 PCs receive the strongest inhibition. Here, we quantify the RC asymmetry in inhibitory strength evoked at rostral vs. caudal stimulation sites. Inhibition was averaged over all rostral (red rectangle in Fig. 1*A1*) or caudal (blue rectangle in Fig. 1*A1*) stimulation sites, shown schematically in Fig. 1*A1* and plotted for each neuron (Fig. 1*A2*). An asymmetric bias index was calculated as the difference in average inhibition from caudal (I_C) vs. rostral (I_R) stimulation sites divided by the sum of the inhibition from both sides (Fig. 1*A3*). By this metric, solely caudal inhibition produces a bias value of +1, while −1 corresponds to rostral inhibition. The distributions of RC bias were calculated for each neuron class (Fig. 1 *B2*, *C2*, and *D2*). Consistent with previous findings (28), L2 PCs and L3 PCs received significantly more inhibition on average from caudal sites vs. rostral sites (L2 bias: 0.21 ± 0.07, $P = 0.014$, $n = 14$, L3 bias: 0.20 ± 0.05, $P = 0.001$, $n = 21$, bias ≠ 0, one-sample t test) (Fig. 1 *C2* and *D2*). Thus, inhibitory circuitry alone is sufficient to reproduce asymmetric inhibition of PCs along the RC axis. However, average inhibitory bias did not differ significantly from 0 in SL (SL bias: 0.16 ± 0.10, $P = 0.11$, $n = 15$) (Fig. 1*A2*). Only one-half ($n = 8$) of SL cells received caudally biased inhibition (bias > 0), and the remainder ($n = 7$) received predominantly rostrally biased inhibition (bias < 0). Since the strength of inhibition varies by layer (31), we also calculated RC bias for each layer (Fig. 1 *B3*, *C3*, and *D3*). All three classes of excitatory neuron, including SL cells, received significant caudally biased inhibition from L3. These findings suggest that L3 inhibitory interneurons, which are recruited by recurrent activity (32, 33), are primarily responsible for asymmetric inhibition in APC. Furthermore, L2/3 PCs that partake in recurrent circuits receive strong asymmetric inhibition from L3. In contrast, SL cells participate primarily in afferent circuits (27, 31, 34) and receive weak inhibition from L3 (31) that is insufficient to bias inhibition across the population.

Synaptic Mechanisms Underlie Stronger Inhibition in Caudal PCs. One interpretation of these findings is that caudally located PCs receive stronger inhibition than rostral PCs. To investigate this possibility, we compared local inhibitory strength in RC PC pairs ($n = 19$) separated by (100–1,000 μm) distances along the ~1.5-mm RC axis in L3 (Fig. 2*A*). To activate local interneuron populations, the 70-μm light spot was focused on the soma of the recorded rostral or caudal PC. Under these conditions, caudal PCs received significantly stronger inhibition (4.18 ± 0.90 pA) than rostral PCs (2.60 ± 0.68 pA, $P = 0.002$, paired t test) (Fig. 2*B*). Moreover, as the distance between rostral and caudal PCs increased, the difference in inhibitory strength increased (slope: 5.8 ± 2.1 pA/mm, $P = 0.013$, $F = 7.66$, $r = 0.56$) (Fig. 2*C*). Finally, across the population of PCs, inhibitory strength increased with soma location relative to the rostral start of the LOT in the sagittal slice (slope: 5.4 ± 1.3 pA/mm, $P = 0.0003$, $n = 27$, $F = 17.73$, $r = 0.64$) (Fig. 2*D*). Thus, inhibition onto PCs increases between rostral and caudal locations over a spatial scale of >1.0 mm along the RC axis of APC.

RC differences in sIPSC frequency (hertz) or amplitude (picoampere) could indicate whether RC differences in evoked inhibition have a presynaptic or postsynaptic locus, respectively. We recorded mini IPSCs (mIPSCs; in 1 μM TTX, $n = 15$ PCs) or sIPSCs (no TTX, $n = 26$ PCs) in PCs located at the L2/3 border. We did not find significant differences between mIPSC and sIPSC amplitude (mIPSC: 16.8 ± 1.5 pA, sIPSC: 15.6 ± 0.8 pA, $P = 0.81$) or frequency (mIPSC: 9.8 ± 0.9 Hz, sIPSC: 8.7 ± 0.6 Hz, $P = 0.69$, unpaired t tests) and hereafter, group these data as sIPSCs. To investigate the mechanisms underlying asymmetric inhibition, we compared sIPSC amplitude and frequency in rostral ($n = 21$) vs. caudal ($n = 20$) PCs. Whenever possible, RC pairs of PCs ($n = 16$) were recorded in the same slice, matched by laminar depth, and separated by a minimum of 600 μm. PCs were recorded at +30 and −70 mV to isolate sIPSCs and sEPSCs, respectively, as shown for an example pair in Fig. 3 *A1* and *A2*. The number of sIPSCs did not differ between pairs of rostral and caudal neurons (rostral: 1,938 ± 275 IPSCs per neuron, caudal: 1,881 ± 213 IPSCs per neuron, $P = 0.74$, paired t test, $n = 16$). The sIPSC amplitude distributions were significantly positively skewed ($P << 0$, Shapiro–Wilk test), but the degree of skew did not differ between rostral and caudal cells (skew: rostral: 2.0 ± 0.3, caudal: 1.7 ± 0.1, $P = 0.23$, paired t test, $n = 16$). In 14 of 16 pairs, sIPSC amplitudes were significantly greater in the caudal vs. rostral PC [$P = 0.000–0.002$, Mann–Whitney U test (MWU) test] (black solid lines in Fig. 3*B*). In one pair, IPSCs were significantly greater in the rostral PC (red line in Fig. 3*B*); in the other, sIPSCs did not significantly differ (dashed line in Fig. 3*B*). Across all pairs, the average sIPSC amplitude was significantly stronger in caudal PCs (19.0 ± 1.3 pA) vs. rostral PCs (14.0 ± 0.8 pA, $P = 0.002$, paired t test) (Fig. 3*B*). Likewise, the average sIPSC amplitude for all caudal PCs (18.6 ± 1.1 pA, $n = 20$) was significantly greater than rostral PCs (13.8 ± 0.6 pA, $n = 21$, $P = 0.0004$, unpaired t test). In contrast, the frequency of sIPSCs did not differ between rostral (8.3 ± 0.5 Hz, $n = 21$) and caudal (9.6 ± 0.9 Hz, $n = 20$) PCs in either unpaired ($P = 0.2$) or paired ($n = 16$, $P = 0.43$, t test) comparisons. Bath application of the GABA$_A$ receptor antagonist Gabazine (GZ; 5–10 μM) significantly decreased sIPSC amplitude [Pre: 15.3 ± 3.6 pA, GZ: 2.4 ± 0.14 pA, $P = 0.01$, nondirectional Wilcoxon signed ranks test (WSR)] and frequency (Pre: 7.8 ± 1.8 Hz, GZ: 0.64 ± 0.16 Hz, $P = 0.005$, nondirectional WSR, $n = 8$) (Fig. 3 *C1* and *C2*). Overall, these findings suggest that stronger caudal inhibition has a postsynaptic locus.

We have previously shown that evoked inhibition dominates excitation in APC (31). Likewise, sIPSCs are significantly stronger than sEPSCs recorded in the same neuron (rostral PCs: sIPSC:
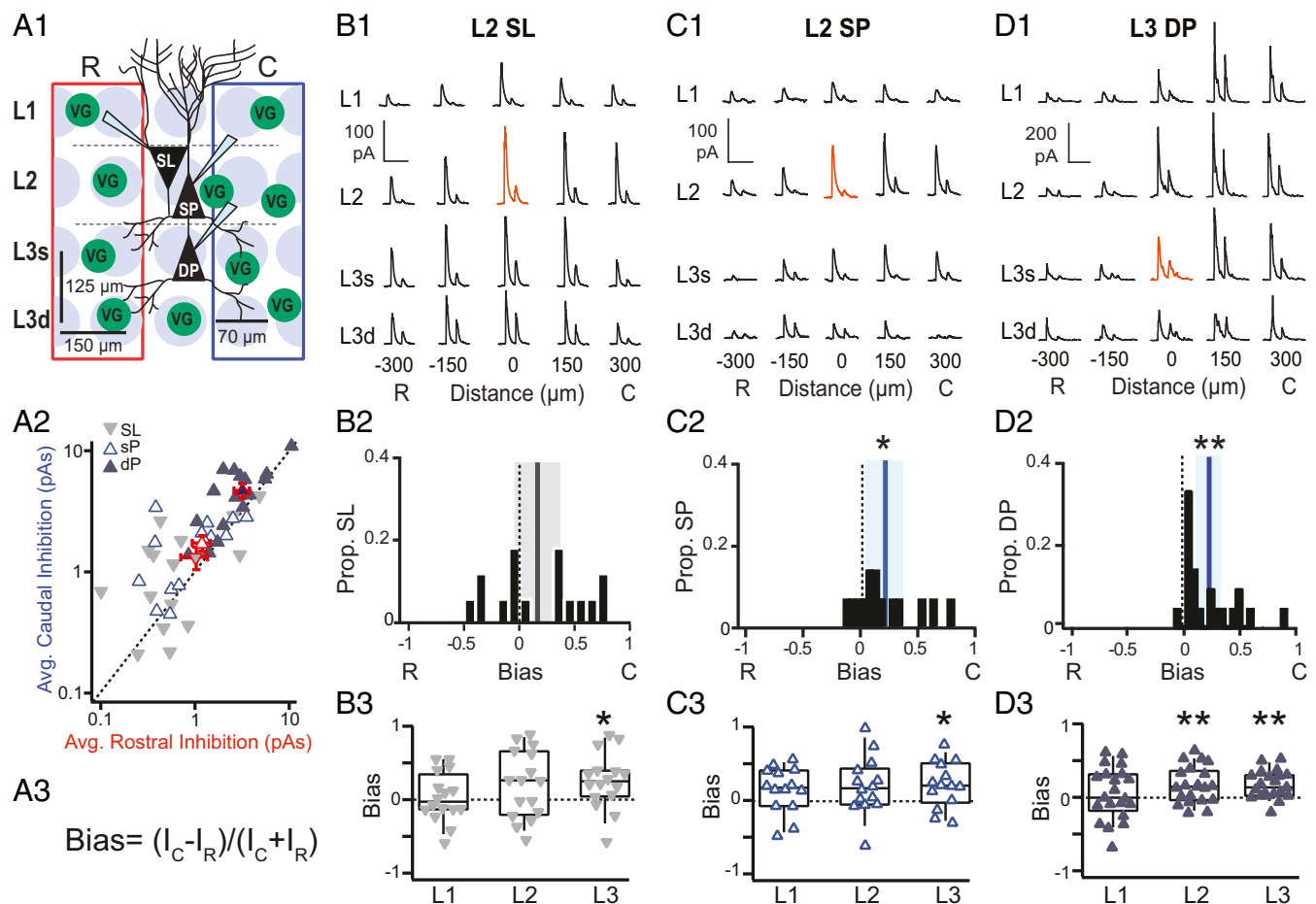
Fig. 1. Caudally biased, asymmetric inhibition within recurrent circuitry of APC. (*A1*) Schematic of the grid stimulation paradigm for excitatory neurons: L2: SL cells and superficial PCs (L2 SP); L3: deep PCs (L3 DP). VG indicates interneuron expressing ChR2 under VGAT promoter. Red or blue rectangles encompass sites included in the average of rostral or caudal inhibition, respectively. C, caudal; R, rostral. (*A2*) Average rostral vs. caudal inhibition (red and blue rectangles, respectively, in *A1*) for each cell class. Filled blue triangles, L3 PC; inverted gray triangles, SL; open blue triangles, L2 PC. (*A3*) Equation for Bias metric. I is the average inhibition across caudal (I_C) or rostral (I_R) sites. Bias is calculated either over all layers as in shown *A1* or by layer as in *B3*, *C3*, and *D3*. In L3, superficial (L3s) and deep layers (L3d) are combined as a single layer. Bias is bounded between −1 and 1. Negative values correspond to greater average inhibition from rostral sites, while positive values correspond to greater inhibition from caudal sites. (*B1*) IPSCs recorded during focal light stimulation at each grid location in a representative SL cell. Red trace indicates the location of the recorded cell. (Scale bars: vertical, 100 pA; horizontal, 200 ms.) (*B2*) SL bias values of inhibition averaged across all layers (*A1*). The black line indicates mean bias, and gray shading indicates 95% confidence intervals. SL population bias was not asymmetric and did not significantly differ from zero. (*B3*) SL bias values calculated for each layer (box, bottom 25%, middle 50%, and top 75%; whiskers, bottom 10% and top 90%). SL cells receive significant caudally biased inhibition only from L3. *$P < 0.05$ (one-sample *t* test). (*C1–C3* and *D1–D3*) Descriptions are the same as in *B1–B3*. (*C1*) IPSCs recorded from a representative L2 PC. (Scale bars: vertical, 100 pA; horizontal, 200 ms.) (*C2*) Bias values for inhibition averaged across all layers (*A1*). The blue line indicates mean bias, and blue shading indicates 95% confidence intervals. L2 PCs receive stronger inhibition from caudal vs. rostral sites. *$P < 0.05$ ($n = 14$, one-sample *t* test). (*C3*) L2 PC bias values calculated for each layer. L2 PCs receive significant caudally biased inhibition from L3. *$P < 0.05$ (one-sample *t* test). (*D1*) IPSCs recorded from a representative L3 PC. (Scale bars: vertical, 200 pA; horizontal, 200 ms.) (*D2*) L3 PC bias values for inhibition averaged across all layers (*A1*). L3 PCs receive stronger inhibition from caudal vs. rostral sites. **$P < 0.01$ ($n = 21$, one-sample *t* test). (*D3*) L3 PC bias values calculated for each layer. L3 PCs receive significant caudally biased inhibition from interneurons in L2 and L3. C, caudal; R, rostral. **$P < 0.01$ (one-sample *t* test).

14.9 ± 0.9 pA, sEPSC: 8.8 ± 0.6 pA, $P = 0.0005$, $n = 14$; caudal PCs: sIPSC: 19.6 ± 1.4 pA, sEPSC: 8.9 ± 0.5 pA, $P = 1.5E-10$, $n = 15$, ANOVA) (Fig. 3*D*). However, sEPSC amplitudes did not differ between rostral and caudal PCs ($P = 0.99$, ANOVA) (Fig. 3*D*). Moreover, sEPSC frequency did not differ along the RC axis or differ with respect to sIPSC frequency (rostral PCs: sIPSC 8.3 ± 0.8 Hz, sEPSC: 8.2 ± 1.3 Hz, caudal PCs: sIPSC: 9.0 ± 1.0 Hz, sEPSC: 7.8 ± 0.9 Hz, $P = 0.44$–0.99 all comparisons, ANOVA) (Fig. 3*E*). The lack of RC differences in sEPSC amplitude or frequency is consistent with previous findings that intracortical excitation does not vary along the RC axis (23). Given uniform excitation and asymmetric inhibition, it is not surprising that caudal PCs have a significantly lower average excitation to inhibition (E:I) ratio than rostral PCs (caudal: 0.48 ± 0.03, $n = 15$, rostral: 0.64 ± 0.04, $n = 14$, $P = 0.002$, unpaired *t* test) (Fig. 3*F*). This suggests the

imbalance between inhibition and excitation increases along the RC axis. However, we also find that sEPSC and sIPSC amplitudes are positively correlated in caudal PCs ($P = 0.024$, $F = 3.71$, $r = 0.57$, $n = 15$) but not rostral PCs ($P = 0.095$, $F = 2.72$, $r = 0.46$, $n = 14$) (Fig. 3*G*). Thus, excitation and inhibition seem to covary on a cell-by-cell basis in caudal APC. This finding suggests that postsynaptic mechanisms, such as synaptic plasticity, may underlie correlated changes in excitatory and inhibitory strength in caudal PCs. Finally, in PCs from across the RC axis ($n = 13$), optogenetically evoked inhibition (VGAT-ChR2) was correlated with sIPSC amplitude ($P = 0.03$, $F = 3.20$, $r = 0.52$) (Fig. 3*H*).

Rostrally Biased Spatially Asymmetric Inhibition of Interneurons. Since PCs are only part of a larger APC network, we endeavored to determine if stronger caudal inhibition is a general feature
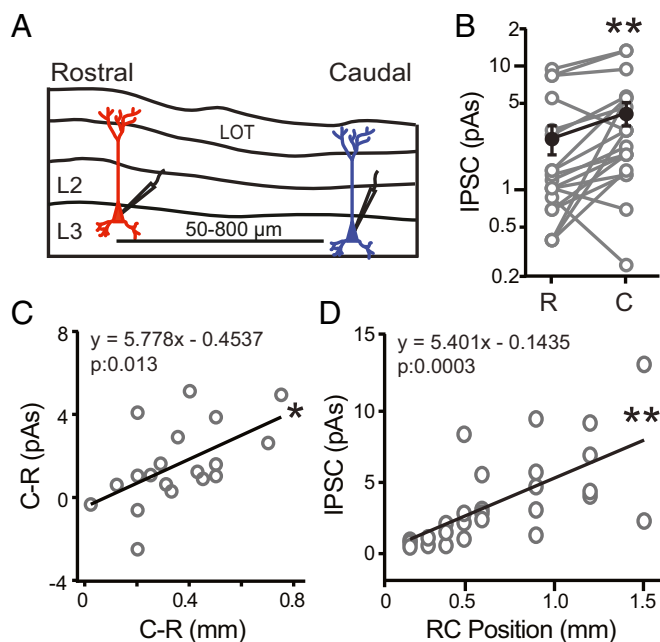
Fig. 2. Caudal PCs receive stronger inhibition than rostral PCs. (A) Schematic of L3 PC pairs recorded in sagittal slices of APC from VGAT-ChR2 mice. Rostral (red) and caudal (blue) PCs were separated by 50–800 μm. Local interneuron circuits surrounding each PC were activated using a 70-μm-diameter light spot aimed at the PC soma. (B) For recordings in the same slice, the caudal (C) neuron of a pair receives stronger inhibition than the rostral (R) neuron. **$P < 0.01$ ($n = 19$ pairs, paired t test). (C) The difference in inhibition (picoamperes · seconds) between the caudal (C) and rostral (R) cell in each pair plotted against the difference in RC distance between the two cells. As the distance between the two cells increases, the difference in inhibition significantly increases. *$P < 0.05$ (linear regression, $n = 19$ pairs). (D) Inhibitory strength vs. RC position of L3 PCs relative to the rostral start of the LOT in the sagittal slice. Inhibition significantly increases with RC position. **$P < 0.01$ (linear regression, $n = 27$).

of APC. We investigated the laminar and RC spatial profiles of inhibition onto L1–L3 interneurons using grid stimulation of VGAT-ChR2 interneurons. Examples of evoked IPSCs recorded in L1–L3 interneurons are shown in Fig. 4 *A1*, *B1*, and *C1*, respectively. Interneurons in L1 (bias: -0.02 ± 0.07, $P = 0.76$) (Fig. 4*A2*) and L2 (bias: 0.03 ± 0.08, $P = 0.67$) (Fig. 4*B2*) did not receive consistently biased inhibition. In addition, L1 and L2 interneurons receive the strongest inhibition primarily from sites in superficial layers, with no significant variation in average inhibition or bias between layers (*SI Appendix*, Fig. S1). Surprisingly, L3 interneurons receive stronger inhibition from rostral sites than caudal sites, resulting in negative bias values (-0.12 ± 0.05, $P = 0.03$, one-sample t test) (Fig. 4*C2*). Furthermore, L3 interneurons receive the strongest inhibition from L3 stimulation sites (3.6 ± 0.5 pA) vs. L2 (2.1 ± 0.4 pA, $P = 0.03$) or L1 sites (1.1 ± 0.3 pA, $P = 0.0001$, ANOVA) (Fig. 4*D1*). Finally, rostrally biased inhibition of L3 interneurons is localized within L3 (L3 bias: -0.14 ± 0.05, $P = 0.0098$, one-sample t test) (Fig. 4*D2*). Thus, L3 interneurons and L3 PCs experience opposing spatial profiles of inhibition—the rostrally biased inhibition of L3 interneurons significantly differs from the caudally biased inhibition of L3 PCs ($P = 0.0001$, unpaired t test) (Fig. 4*E*). Furthermore, since both PCs and L3 interneurons show the strongest inhibitory asymmetries as a result of light activation of L3 interneurons, we propose that recurrently recruited L3 circuits underlie asymmetric inhibition.

How do inhibitory circuits implement opposing RC inhibitory asymmetries? We compared sIPSCs in rostral (Fig. 5 *A1* and *A2*) ($n = 15$) vs. caudal (Fig. 5 *B1* and *B2*) ($n = 15$) interneurons. In

contrast to PCs, sIPSC frequency (caudal: 4.9 ± 0.9 Hz, rostral: 8.1 ± 0.7 Hz, $P = 0.008$ Welch's t test) (Fig. 5*C*) is significantly greater in rostral interneurons vs. caudal interneurons. The amplitude of sIPSCs did not significantly differ between rostral and caudal interneurons (caudal: 15.6 ± 3.0 pA, rostral: 16.4 ± 1.5 pA, $P = 0.81$, unpaired t test) (Fig. 5*D*). This remains significant even if the outlier (Fig. 5*D*) is removed ($P = 0.10$, unpaired t test). These findings suggest that (*i*) rostrally biased inhibition of interneurons potentially has presynaptic locus and that (*ii*) different mechanisms underlie asymmetric inhibition of PCs and L3 interneurons.

One possibility is that different interneuron classes underlie opposing inhibitory asymmetries in L3 PCs and interneurons. Since the majority (∼85%) of interneurons in L3 express PV, SST, and/or calbindin (CB) (35), we investigated the RC distributions of these three interneuron classes. We found that SST cells decreased in density along the RC axis (Fig. 6 *A1–A4*), but the densities of PV and CB cells did not vary with RC distance (*SI Appendix*, Fig. S2). L3 SST cells were identified as tdTom(+) somas and counted in coronal sections from SST-Ai14 mice (Fig. 6*A1*). The density of SST cells in each section was normalized to the most rostral section [∼2.46 mm from Bregma (36)]. The normalized density vs. RC distance was then linearly fit to obtain the slope of the change in density per millimeter (Fig. 6 *A2–A4* and *SI Appendix*, Table S1). SST cell densities consistently decreased along the RC axis as shown for a single mouse (Fig. 6*A2*) and in the average density across all mice (Fig. 6*A3*) (slope: -0.25 ± 0.03 mm^{-1}, $P < 0.0001$). In the majority of mice ($n = 5/7$), linear fits of SST cell density vs. RC distance had significantly negative slope values (mean slope $\neq$ 0: -0.20 ± 0.04 mm^{-1}, $P = 0.002$, MWU test) (Fig. 6*A4*). The distributions of CB and PV cells did not significantly vary along the RC axis of APC (*SI Appendix*, Fig. S2 and Table S1). Since none of these interneuron classes increase in density along the RC axis, it is unlikely that caudally biased inhibition of PCs can be simply explained by changes in the density of SST, CB, or PV cells. However, a greater rostral vs. caudal density of SST cells is consistent with increased sIPSC frequency in rostral vs. caudal interneurons. Thus, it is possible that SST cells underlie the rostrally biased inhibition of interneurons.

We have previously shown that SST cells inhibit the majority of L3 interneurons as well as L3 PCs in APC (37). To test if the high rostral density of SST cells provides rostrally biased inhibition, we selectively expressed ChR2 in SST cells (SST-ChR2) (*Methods*) and repeated grid stimulation while recording L3 interneurons and L3 PCs (Fig. 6*B*). As predicted, SST cells provided rostrally biased inhibition to L3 interneurons (bias: -0.11 ± 0.04, $P = 0.02$, $n = 22$) (Fig. 6 *C1* and *C2*), and the distribution of rostral bias values did not significantly differ from bias values in VGAT-ChR2 mice (-0.12 ± 0.05, $P = 0.84$, unpaired t test). Thus, it is highly likely that a higher rostral density of SST cells underlies rostrally biased inhibition of L3 interneurons.

In contrast, the spatial profile of SST cell-mediated inhibition of L3 PCs was bidirectional, producing a distribution of bias values that was neutral over the population (bias = 0: 0.06 ± 0.08, $P = 0.38$, one-sample t test, $n = 14$) (Fig. 6*D2*). One half of the PCs received rostrally biased inhibition ($n = 7/14$) (Fig. 6 *D1* and *D2*), consistent with SST cell density. However, since only 10% of L3 PCs ($n = 2/20$) showed rostrally biased inhibition in VGAT-ChR2 mice, it is unlikely that rostrally biased SST inhibition significantly affects asymmetric caudal inhibition of PCs. The other one-half of the PCs received caudally biased inhibition from SST cells, despite a lower caudal density of SST cells. Thus, SST-to-PC inhibitory synapses could participate in caudally biased inhibition. However, since only 50% of PCs showed caudally biased SST-mediated inhibition, it is also unlikely that SST cells can solely mediate caudally biased inhibition. Furthermore, maximum inhibition of PCs in SST-ChR2 mice (4.77 ± 0.89 pA) was only
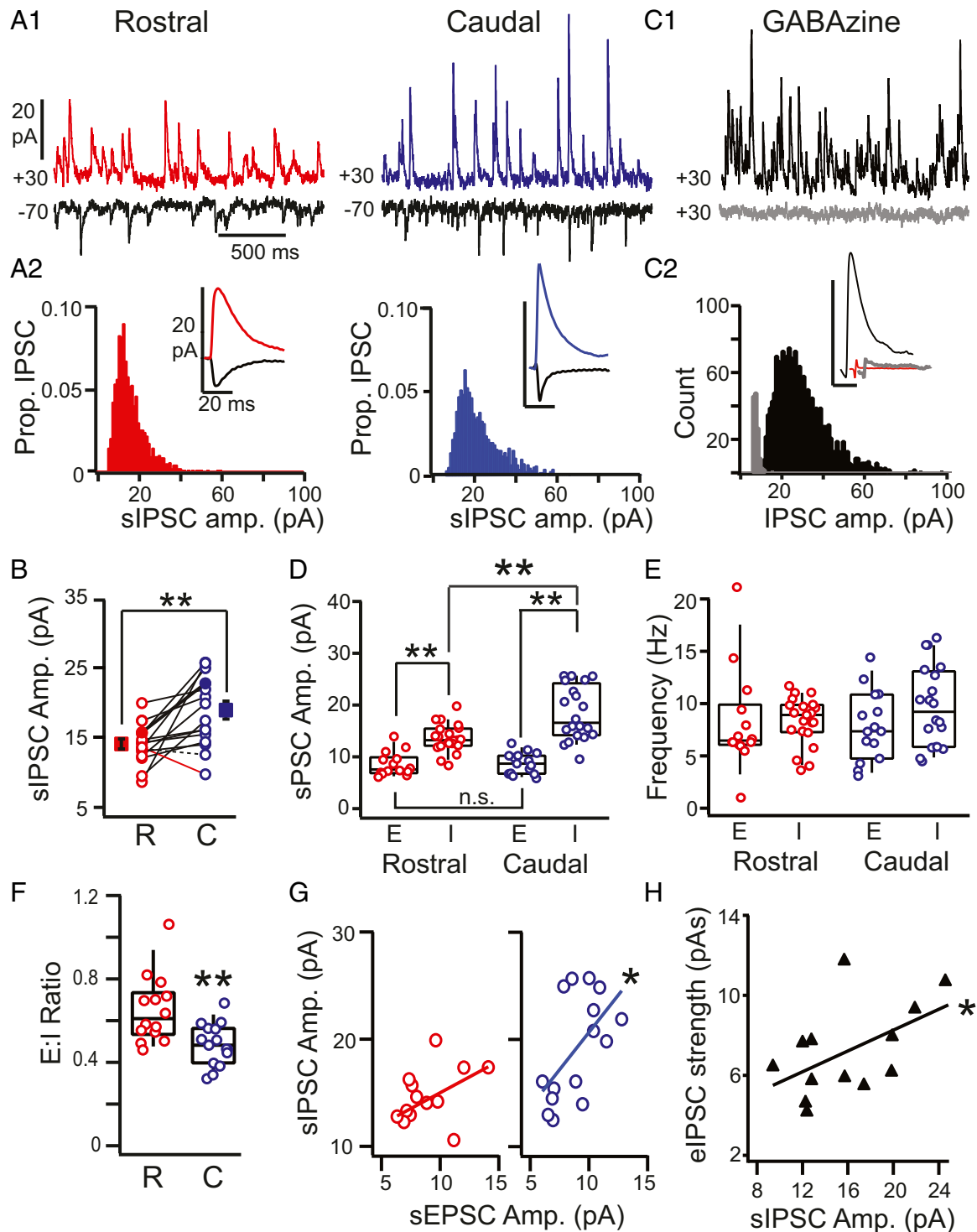
Fig. 3. Comparison of sIPSCs in rostral vs. caudal PCs. (*A1*) Representative smoothed traces (details are in *SI Appendix, SI Methods* and Fig. S4) showing sEPSCs (black) and sIPSCs in rostral (red; *Left*) and caudal (blue; *Right*) PCs recorded in the same slice. (*A2*) The amplitude distributions of sIPSCs recorded in the neurons shown in *A1*. (*Insets*) Average sEPSCs (black) and sIPSCs recorded in the rostral (red) and caudal (blue) PCs shown in *A1*. (*B*) Average sIPSC amplitudes for all RC cell pairs. In the majority of pairs, sIPSCs were stronger in the caudal (C) PC (solid black lines; *P* < 0.05, unpaired *t* test). In one pair, the rostral (R) PC had stronger IPSCs (red line; *P* < 0.05). One pair did not significantly differ (dashed black line). The average sIPSC amplitude across all caudal PCs was significantly greater than rostral PCs. **P* < 0.01 (paired *t* test). (*C1*) Traces showing representative sIPSCs (black) blocked by GZ (5 µM; gray). (*C2*) sIPSC amplitude distributions before (black) and after (gray) GZ. (*Inset*) Average sIPSC before (black) and after (gray) GZ; the red line is the average nonevent that corresponds to baseline noise. Traces are offset for visibility. (*D*) sEPSC (E) and sIPSC (I) amplitude in rostral (red) and caudal (blue) PCs. **P* < 0.01 (ANOVA). (*E*) sEPSC (E) and sIPSC (I) frequency in rostral (red) and caudal (blue) PCs. (*F*) Ratio of sEPSC to sIPSC amplitude (E:I ratio) in rostral vs. caudal PCs. **P* < 0.01 (*t* test). (*G*) sIPSC amplitude vs. sEPSC amplitude in rostral (*Left*; red) and caudal cells (*Right*; blue). **P* < 0.05. (*H*) Evoked IPSC amplitude vs. sIPSC amplitude is positively correlated in PCs. **P* < 0.05.
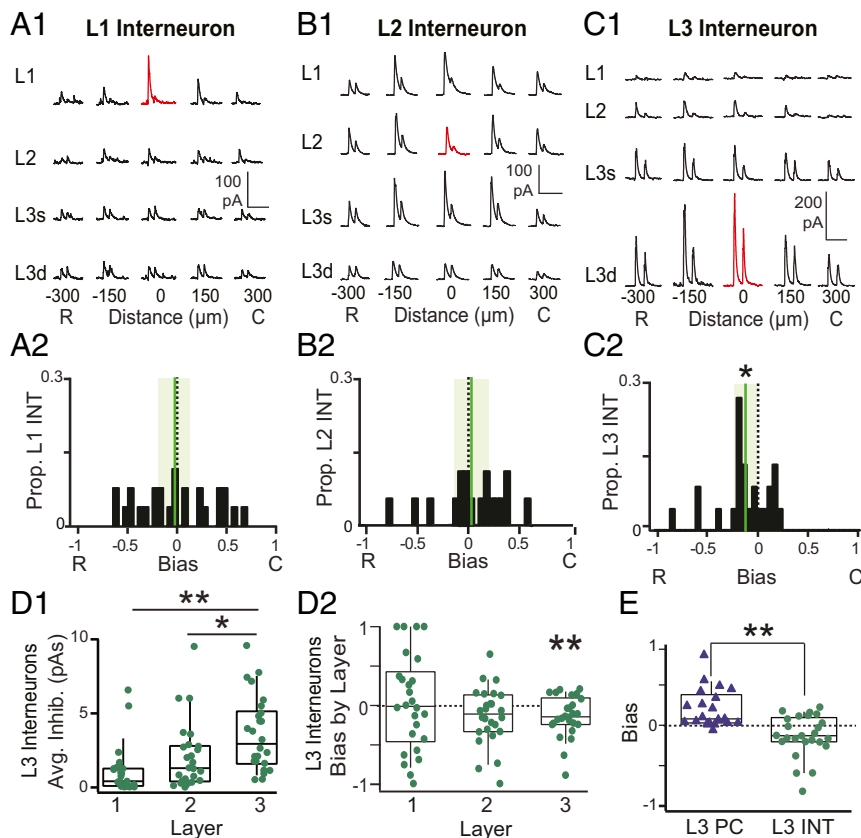
Fig. 4. Rostrally biased, asymmetric inhibition of L3 interneurons. (*A1*) IPSCs recorded during focal light stimulation at each grid location in a representative L1 interneuron (INT). Red traces indicate location of recorded cell. (*A2*) The distribution inhibitory bias values for the L1 INTs. The mean (green vertical line) does not differ from zero; the shaded green bar corresponds to the 95% confidence interval around the mean. (*B1*) IPSCs recorded during focal light stimulation at each grid location in a representative L2 INT. (*B2*) The distribution inhibitory bias values for the L2 INTs. The mean bias does not differ from zero. (*C1*) IPSCs recorded from a representative L3 INT. (Note the change in the vertical scale bar to 200 pA. Horizontal scale bars: *A1–C1*, 200 ms.) (*C2*) Asymmetric distribution of negative bias values in L3 INT indicates stronger inhibition from rostral vs. caudal sites. *$P < 0.05$ ($n = 25$, one-sample t test). (*D1*) L3 interneurons receive significantly stronger inhibition from stimulation sites in L3 than L1 or L2. *$P < 0.05$ (ANOVA); **$P < 0.01$ (ANOVA). (*D2*) Bias values calculated for each layer for L3 interneurons. L3 interneurons receive significant rostrally biased inhibition from other L3 interneurons. **$P < 0.01$ (one-sample t test). (*E*) The bias values of L3 PCs (blue triangles) significantly differed from L3 INTs (green circles). C, caudal; R, rostral. **$P < 0.01$ (unpaired t test).

one-half of the strength of inhibition in VGAT-ChR2 mice (8.63 ± 0.84 pA, $P = 0.003$, unpaired t test). Altogether, these findings suggest that additional interneuron circuits are required for the full expression of caudally biased, asymmetric inhibition in PCs.

In summary, we show that postsynaptic mechanisms underlie caudally biased inhibition of PCs. This inhibition likely arises from more than a single class of interneurons. Conversely, rostrally biased inhibition of L3 interneurons is mediated by rostrally biased distributions of SST cells. These opposing spatial asymmetries in inhibition provide evidence to support RC differences in APC inhibitory circuits that could underlie functional differences in rostral vs. caudal network processing of odors.

Discussion

Inhibition plays a critical role in the processing and representation of sensory information in the cortex (38). In APC, inhibition balances excitation (31, 32, 39), narrows synaptic integration windows (23, 32, 33, 39–41), supports oscillatory activity, and sharpens odor tuning (25, 42–44). It is assumed that the functional contribution of inhibition to olfactory processing is uniform across the piriform cortex. In this study, we investigate the RC spatial patterning of evoked and spontaneous inhibition in APC. We reproduce previous findings of caudally biased inhibition of PCs (28) and provide three major advances with respect to the underlying synaptic and circuit mechanisms of

asymmetric inhibition. First, we show that inhibitory asymmetries are a feature of circuits recruited by recurrent activity in APC. Specifically, L3 interneurons provide asymmetric inhibition to all excitatory neurons as well as other L3 interneurons. However, only PCs and L3 interneurons receive consistently asymmetric inhibition across their respective populations. Neurons preferentially recruited by afferent input, such as SL cells and superficial L1 and L2 interneurons (31–34, 45, 46), do not receive or provide consistently asymmetric inhibition. Second, although the strong caudal bias in inhibition of PCs had been previously reported, an opposing rostral bias in inhibition of L3 interneurons is a surprising finding. Third, these opposing spatial asymmetries are supported by different mechanisms. Caudally biased inhibition of PCs arises from postsynaptic mechanisms that enhance inhibitory synaptic strength in caudal PCs. Rostrally biased inhibition of interneurons is mediated by SST interneurons that decrease in density along the RC axis. Altogether, our findings suggest that recurrent inhibitory circuits comprise a dimension for RC spatial organization and odor processing within APC.

Mechanisms of Asymmetric Inhibition in PCs. Given the uniform profile of afferent (20–22) and recurrent (23, 24) excitation in APC, it is surprising that inhibitory strength changes along the RC axis. We have previously shown that recurrently recruited inhibition is substantially stronger than excitation in PCs (31).
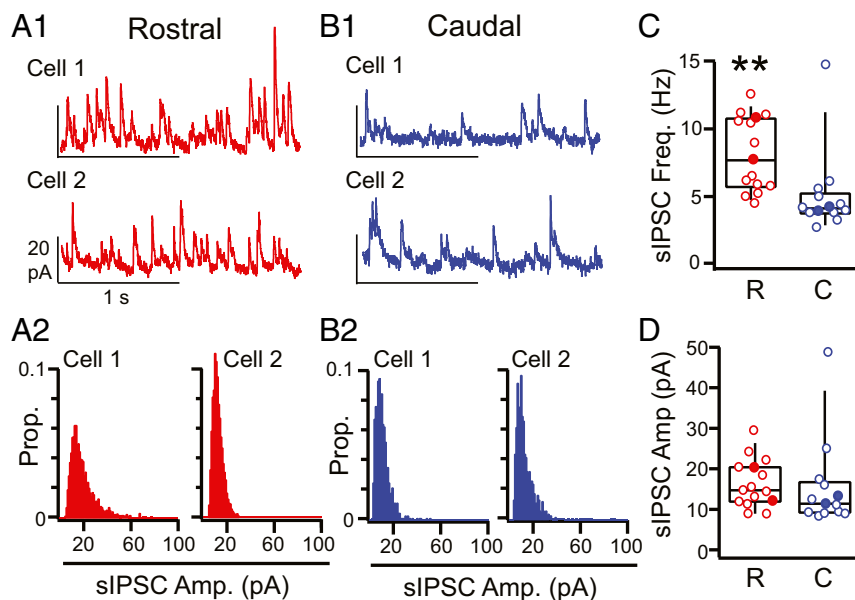
Fig. 5. Comparison of sIPSCs in rostral vs. caudal L3 interneurons. (*A1*) Representative traces and (*A2*) sIPSC amplitude histograms from two different rostral L3 interneurons (red). (*B1*) Representative traces and (*B2*) sIPSC amplitude histograms from two different caudal L3 interneurons (blue). (*C*) sIPSC frequency significantly differed in rostral (R; red) vs. caudal (C; blue) interneurons (box: bottom 25%, middle 50%, and top 75%; whiskers: bottom 10% and top 90%). Filled circles indicate data from neurons shown in *A* and *B*. **$P < 0.01$ (Welch's t test). (*D*) sIPSC amplitude in rostral (R; red) vs. caudal (C; blue) interneurons (box: bottom 25%, middle 50%, and top 75%; whiskers: bottom 10% and top 90%). Filled circles indicate data from neurons in *A1*, *A2*, *B1*, and *B2*.

However, increased caudal inhibition implies that the ratio of excitation to inhibition further changes with RC space. Our analysis of sEPSCs and IPSCs reveals that E:I ratios differ in rostral and caudal APC. Specifically, we show that sEPSC amplitudes do not vary across the RC axis, while sIPSC amplitudes are greater in caudal vs. rostral PCs. Thus, despite uniform excitation, caudal PCs may need to pool a greater number of excitatory inputs to reach threshold. Interestingly, we also find that sIPSC amplitudes scale with sEPSCs in caudal but not rostral PCs. An alternate possibility is that caudal cells have greater reliance on the temporal correlation of stronger inputs to reach threshold.

Since the sIPSC frequency in PCs does not vary along the RC axis, it is unlikely that increased density of inhibitory connections underlies asymmetric inhibition of PCs. Rather, increases in sIPSC strength suggest that postsynaptic plasticity mechanisms act to globally increase inhibition across caudal PCs (47) as well as to selectively increase inhibition relative to excitation individual PCs (48). Synaptic plasticity mechanisms have long been proposed to underlie the synthesis of odor information in mixtures into a single percept (49–51). Although, the representation of odor gestalts has been attributed to PPC (17, 52), this does not preclude the possibility that odor percepts are sequentially processed along the RC axis of APC. Caudal APC could play a greater role than rostral APC in the early stages of fusing odor information. As a result, asymmetric inhibition of PCs in APC could be a product of inhibitory plasticity in response to increases in synaptic strength and/or the greater pooling of inputs during consolidation of odor mixture information.

Spatial Patterning of SST Cell-Mediated Inhibition. We have previously shown that SST interneurons inhibit a variety of L3 interneuron subtypes as well as PCs in APC (37). Here, we find that SST cells decrease in density along the RC axis and provide rostrally biased inhibition to interneurons and bidirectional inhibition of PCs. It has been previously shown that SST cell inhibition has a subtractive effect on PC odor tuning and a divisive effect on interneuron tuning (44). In addition, SST cells project to L1 and inhibit PC dendrites (32, 37), which could gate

synaptic plasticity (53–55). Thus, spatial variation in SST-mediated inhibition could lead to variation in odor tuning or plasticity across the RC extent of APC.

Despite the prominent role that inhibition plays in shaping piriform responses, few studies have addressed circuits that modulate inhibition in APC (42, 44). In neocortex, SST interneurons partake in circuits that disinhibit PCs by targeted inhibition of inhibitory interneurons (56–63). However, disentangling inhibitory vs. disinhibitory effects of SST cells on PCs is challenging. We find that SST cells can directly provide rostrally biased inhibition due to greater rostral density of SST cells or caudally biased inhibition through SST-to-PC inhibitory synaptic plasticity. Indirectly, rostral disinhibition via SST–interneuron–PC circuits could also increase caudal bias. Furthermore, there are three different classes of SST cells in APC (37) that could differ with respect to inhibition of PCs and/or interneurons and RC density. Targeting SST cells with current genetic strategies does not distinguish these neuron subtypes or inhibitory vs. disinhibitory circuits. Nonetheless, our findings suggest that SST cells could mediate disinhibition of PCs by inhibiting interneurons, and furthermore, disinhibition could vary with SST cell density along the RC axis.

Although we find that two different mechanisms underlie asymmetric inhibition in PCs vs. interneurons, it is interesting that both scenarios could produce stronger inhibition of caudal PCs vs. rostral PCs. Strong inhibition of rostral interneurons through SST–interneuron–PC disinhibitory circuits could produce weak inhibition of rostral PCs compared with caudal PCs. This parallels the stronger inhibition of caudal PCs vs. rostral PCs through postsynaptic plasticity. Why two mechanisms for potentially similar outcomes? One possibility is that the two mechanisms work in concert to enhance RC differences in inhibition. An alternate possibility is that the two mechanisms affect network performance with different timescales and/or context dependencies. Recent studies have shown that SST interneuron activity in neocortex is enhanced by cholinergic modulation (60, 64, 65), and/or engagement in sensory tasks (60, 63, 65, 66). Thus, disinhibition through SST–interneuron–PC

Fig. 6. Spatial profiles of SST cell-mediated inhibition. (*A1*) Representative coronal sections from rostral (0–200 μm; *Left*) and caudal (within last 300 μm; *Right*) APC showing SST-tdTom(+) cells in an L3 region of interest (dashed line). (Scale bar: 500 μm.) (*A2*) Normalized density vs. RC distance for the mouse shown in *A1*. **$P < 0.01$. (*A3*) Normalized density of SST cells vs. distance for all mice (open circles). The average ($\pm$SE; $n = 7$) normalized density of SST cells across mice significantly decreased with RC distance (red circles). **$P < 0.01$. (*A4*) Distribution of slopes from linear fits to data from individual mice. Solid circles indicate significantly negative slopes ($P < 0.05$). The distribution of slope values was significantly nonzero. **$P = 0.002$ (MWU). (*B*) Schematic of the grid stimulation paradigm for L3 PCs and L3 interneurons (INTs) in sagittal sections from SST-ChR2 mice. (*C1*) IPSCs recorded during focal light stimulation at each grid location in a representative L3 INT. The red trace indicates the location of the recorded cell. (Scale bars: vertical, 200 pA; horizontal, 200 ms.) (*C2*) The distribution of bias values for L3 INTs is significantly rostrally biased (cyan line; the shaded region is the 95% confidence interval) and does not differ from VGAT-ChR2 mice (green line, $P = 0.84$, unpaired t test). *$P < 0.05$ (one-sample t test). (*D1*) IPSCs recorded from a representative L3 PC. (Scale bars: vertical, 100 pA; horizontal, 200 ms.) (*D2*) The distribution of bias values in PCs is not asymmetric, and the mean does not differ from zero ($P = 0.38$; cyan line) compared with the positive, caudally biased mean in VGAT-ChR2 mice (green line). C, caudal; R, rostral.

circuits can be flexible and modulated on short, within-session, behavioral timescales compared with long-term changes in synaptic plasticity over the course of learning. Overall, our findings show that SST cells inhibit both PCs and interneurons and play a role in the RC patterning of inhibition in APC. However, there is still considerable effort needed to assign specific roles for SST cells in inhibition or disinhibition during odor processing.

Functional Roles for RC Asymmetries in Olfactory Processing. Finally, it is conceivable that inhibitory asymmetries reflect regional specializations along the RC axis of APC. An intriguing possibility is that RC patterning in inhibitory circuits interacts with other identified RC asymmetries in APC. For example, tufted cell afferents are limited to the rostral–ventral APC (21), and the overall density of OB afferents decreases along the RC extent of the LOT. Alternatively, there is rostral bias in projections from the APC to the OB (67) and the orbitofrontal cortex (OFC) (14, 68), whereas projections to agranular insula (AI) are from caudal APC (68). Projections from PPC (69) and frontal cortex (14, 70) to APC also show RC biases. We find that inhibitory asymmetries are a feature of recurrent rather than afferent circuitry in APC and occur on a spatial scale that is consistent with projections between APC and higher brain centers, like AI, OFC, and PPC. One speculation is that variation in inhibition across the RC axis mediates these higher-order interactions. Conversely, it is possible that RC patterning in disinhibitory or inhibitory circuits could confer susceptibility or protection to pathology, such as epilepsy (71, 72). Ultimately, it remains to be determined what roles the various sources of RC asymmetry play in the neural processing in APC. Nonetheless, our study adds to a growing body of evidence that, despite the lack of a topographic code for odor identity, space is a relevant dimension in APC.

Methods

Mice. A number of transgenic mouse lines and crosses were used in this study. VGAT-ChR2 mice [*VGAT-ChR2*:B6.Cg-Tg(Slc32a1-COP4*H134R/EYFP)8Gfng/J] express ChR2 in all interneurons (73). The *SST-Cre* [B6:Sst<tm2.1(cre)Zjh>/J] mice were crossed with *Ai32* mice [B6;129S-Gt(ROSA)26Sortm32(CAG-COP4*H134R/EYFP)Hze/J] to express ChR2 (SST-ChR2) or Ai14 mice [B6.Cg-Gt(ROSA)26Sortm14(CAG-tdTomato)Hze/J] to express tdTomato (74). All mouse lines were from Jackson Laboratories. All experiments included mice of both sexes.

Slice Preparation. Brain slices of APC were prepared from mice ages P19–P35. The mice were anesthetized with isoflurane and decapitated. The brain was removed and immersed in ice-cold oxygenated (95% O_2, 5% CO_2) artificial cerebral spinal fluid (ACSF) (125 mM NaCl, 2.5 mM KCl, 25 mM NaHCO$_3$, 1.25 mM NaH$_2$PO$_4$, 1.0 mM MgCl$_2$, 25 mM Dextrose, 2.5 mM CaCl$_2$; all chemicals were from Sigma unless otherwise stated). Parasagittal slices (300 μm) were made using a vibratome (Leica Biosystems) in ice-cold ACSF. The slices were transferred to warm ACSF (37 °C) for 30 min and then rested at 20 °C to 22 °C for 1 h before recording (31 °C to 35 °C). All procedures were approved by the University of Pittsburgh Institutional Animal Care and Use Committee.

Electrophysiology. Recordings were obtained from L2/3 PCs and L2 SL cells as well as interneurons in layers 1–3. Neurons were visualized using IR differential interference contrast microscopy (Olympus). Whole-cell, voltage, and current clamp recordings were performed using a MultiClamp 700B amplifier (Molecular Devices). Data were low pass filtered (4 kHz) and digitized at 10 kHz using an ITC-18 (Instrutech) controlled by custom software (Recording Artist; https://bitbucket.org/rgerkin/recording-artist) written in IgorPro (Wavemetrics). Recording pipettes (4–10 MΩ) were pulled from borosilicate glass (1.5-mm o.d.) on a Flaming/Brown micropipette puller (Sutter Instruments). The series resistance (<20 MΩ) was not corrected. Evoked IPSCs were recorded using an intracellular solution consisting of 130 mM K-gluconate, 5 mM KCl, 2 mM MgCl$_2$, 4 mM ATP-Mg, 0.3 mM GTP, 10 mM Hepes, 10 mM phosphocreatine, 0.05% biocytin, and 4.5 μM QX-314. sIPSCs and sEPSCs were recorded using intracellular solution consisting of 100 mM gluconic acid, 5 mM MgCl$_2$, 0.2 mM EGTA, 40 mM Hepes, 2 mM ATP-Mg, 0.3 mM GTP, 7.5 μM QX-314, and 0.05% biocytin titrated to pH 7.2 with

50% Cs-OH. In an additional subset of PCs (n = 12) and interneurons (n = 6), evoked IPSCs were recorded using the Cs-Gluconate internal. Inhibitory asymmetries were consistent across solution and the results were combined. For all neurons, intrinsic subthreshold properties, such as input resistance, and time constant, were assessed using a series of hyperpolarizing and depolarizing current steps (−50 to 50 pA, 1-s duration). Neural identity was confirmed post hoc using intrinsic properties and anatomical analysis of biocytin fills. Neurons that could not be confidently identified as SL cells, PCs, or interneurons were excluded from analysis.

Light Stimulation. Blue light (λ = 460–488 nm, GFP block; Olympus) for optical stimulation was provided by a metal halide lamp (200 W; Prior Scientific) passed through the microscope objective (60×, immersion; Olympus). Light pulses were controlled using a mechanical shutter (Sutter Instruments). The light spot was restricted to an ~70-μm diameter (0.5 mW) using the minimum aperture. To obtain the spatial profile of inhibition, interneurons were focally activated in a 5 × 4-grid pattern while IPSCs were recorded in PCs or interneurons. The horizontal axis of the grid was centered on the recorded neuron, with stimulation sites ranging from −300 μm (rostral) to +300 μm (caudal) at 150-μm increments. The vertical axis ranged from L1 to L3 in 125-μm increments, corresponding to different lamina. Each grid site was stimulated with two light pulses (20-ms duration, 100-ms interpulse interval, 15 s between trials). The 20-ms duration was chosen to reliably evoke at least one spike and rarely, two spikes in response to a single pulse of direct somatic stimulation using the 70-μm spot at 0.5 mW (31). For these stimulation conditions, we find that spike probability drops to less than 40% for stimulation at 150 μm and nearly zero at 300 μm from the soma (*SI Appendix*, Fig. S3 *E1 and E2*). We also find that spike probability (*SI Appendix*, Fig. S3 *E1 and E2*) shows no RC bias and thus, is unlikely to be a source of RC asymmetry. Grids were repeated three to seven times per neuron, and each grid site was stimulated once every 6 min. Since solely inhibitory neurons are activated and there is no evidence of depolarizing inhibition near threshold, polysynaptic responses are unlikely under these recording conditions.

Analysis of Inhibition. In the majority of cells, voltage clamp recordings of IPSCs were performed at holding potentials between 0 to +10 mV. L1 interneurons were the exception and held between 0 and +50 mV. Since we recorded IPSCs in interneurons that expressed ChR2, we used a series of holding potentials (from −70 to +30 mV) to ensure that the ChR2 current reversed in each cell. Interneurons in which ChR2 could not be reversed were excluded. We quantified the potential influence of ChR2 on the measurement of IPSCs by varying holding potential in the absence or presence of the GABA$_A$ receptor antagonist GZ (10 μM) (*SI Appendix*, Fig. S3 *A, B1, and B2*). We find that the presence of ChR2 could lead to an underestimate of IPSC strength by ~24% at 0 mV and 10% at 10 mV. However, since ChR2 currents do not show RC bias (*SI Appendix*, Fig. S3 *C, D1, and D2*), these underestimates are unlikely to contaminate measurement of asymmetric inhibition.

Electrophysiology traces of evoked IPSCs are presented as the average across trials (n = 3–7) for individual neurons. Since evoked IPSCs are population responses, IPSC strength was taken as the area (picoamperes · seconds) under the first IPSC of the pair of light pulses. The second IPSC was not analyzed due to unreliable action potential firing on the second light pulse (31). Average evoked postsynaptic currents (PSCs) with minimum amplitude of 10 pA were included for analyses; smaller PSCs were difficult to distinguish from noise and given a value of zero. The RC bias was taken as the average inhibition from all caudal stimulation sites minus the average inhibition of the rostral sites (Fig. 1 *A1–A3*, red or blue rectangles) divided by the summed inhibition from both sides. The bias metric ranges from −1 (rostral bias) to +1 (caudal bias).

Spontaneous PSCs were accumulated over 2- to 4-min recordings at a holding potential of −70 mV (sEPSCs) or +30 mV (sIPSCs; 5-kHz sampling). PSC detection, amplitude (picoamperes), and frequency (hertz) analyses

were automated using custom software written in IgorPro that combines first derivative thresholds with template matching (75) to identify spontaneous PSCs. Briefly, traces were smoothed using a binomial filter and duplicated for differentiation. The largest PSC events were identified as peaks in the derivative trace that were initially 4 SDs greater than the mean instantaneous slope. These events were averaged to obtain a template PSC that could be scaled for template matching for the remaining smaller putative PSCs. After PSC template selection, the threshold for PSC event detection was decreased to 2 SDs from the mean. Potential PSCs were extracted compared with the template using a mean squared error (MSE) metric. PSCs that were well-fit by the template (low MSE) and a minimum of 5 pA in amplitude were included in the dataset. All datasets were checked by eye to ensure accuracy in PSC selection. A subset of datasets as well as simulated data were used to validate code performance and obtain expected error rates. A detailed description of this analysis code and validation is provided in *SI Appendix, SI Methods* and Fig. S4.

Anatomy. Mice were given an overdose of ketamine-xylazine. Mice were then perfused transcardially (20 mL/min) with 0.1 M sodium phosphate buffer (PB) followed by 200 mL of 4% paraformaldehyde (PFA) in 0.2 M PB. Brains were removed and fixed in 4% PFA overnight at 4 °C, and then, they were transferred to a sucrose solution. Coronal slices (50 μm) were cut using a freezing microtome and maintained in PB before immunochemistry and/or mounting. Primary antibodies were rabbit anti-PV (PV27, 1:1,000; Swant) and rabbit anti-CB D-28K (CB38, 1:1,000; Swant). The secondary antibody was donkey anti-rabbit Alexa Fluor 488 (A21206; 1:500; Life Technologies). Every other section was mounted using fluoromount. Sections were imaged on a Nikon Eclipse-Ci microscope at 4× magnification. Illumination was provided by a mercury lamp (Nikon Intensilight) and delivered through appropriate filter blocks for GFP (495 nm) and tdTomato (585 nm). Light intensity and exposure duration (100–400 ms) were optimized for the first section in a series using automated software (Nikon Elements) and then maintained for ensuing sections. Sections were photographed using a CCD high-definition color camera (Nikon DsFi2).

Cell Counts. Neural densities were quantified as the number of somas per 1 mm^2 in L3 located directly under the LOT in APC. Counts were made in a single focus plane (4× magnification) for each section chosen to maximize the number of cells in focus. Automated counts of somas were obtained based on fluorescence intensity and circularity using Elements Software (Nikon). Two researchers independently verified all counts, with at least one blind to condition. In the event of discrepancy, a third individual, blind to condition, performed counts. Every other coronal section (8–15 sections per animal) was analyzed spanning a minimum of 1 mm along the RC axis. To assess RC spatial patterning, densities in each section were normalized to the most rostral section, corresponding to ~2.46 mm from Bregma (36). For each animal, the slope of the least squares linear regression between normalized density and RC distance was used to quantify spatial patterning.

Statistics. All data are presented as means ± SE unless otherwise stated. Statistical tests were performed using two-tailed, one- or two-sample paired or unpaired Student's t test as appropriate. In cases of unequal variance, a Welch's t test was applied. In cases of small sample sizes (<10) or nonnormal distributions, nonparametric tests were used, including the MWU for unpaired data and the WSR for paired data. For multiple comparisons, we used ANOVA with post hoc Tukey test. All statistical tests are indicated in the text and/or the figures.

1. Mombaerts P, et al. (1996) Visualizing an olfactory sensory map. *Cell* 87:675–686.
2. Mori K, Sakano H (2011) How is the olfactory map formed and interpreted in the mammalian brain? *Annu Rev Neurosci* 34:467–499.
3. Buonviso N, Chaput MA, Scott JW (1991) Mitral cell-to-glomerulus connectivity: An HRP study of the orientation of mitral cell apical dendrites. *J Comp Neurol* 307:57–64.
4. Davison IG, Ehlers MD (2011) Neural circuit mechanisms for pattern detection and feature combination in olfactory cortex. *Neuron* 70:82–94.
5. Davison IG, Katz LC (2007) Sparse and selective odor coding by mitral/tufted neurons in the main olfactory bulb. *J Neurosci* 27:2091–2101.
6. Fried HU, Fuss SH, Korsching SI (2002) Selective imaging of presynaptic activity in the mouse olfactory bulb shows concentration and structure dependence of odor responses in identified glomeruli. *Proc Natl Acad Sci USA* 99:3222–3227.
7. Soucy ER, Albeanu DF, Fantana AL, Murthy VN, Meister M (2009) Precision and diversity in an odor map on the olfactory bulb. *Nat Neurosci* 12:210–220.
8. Spors H, Wachowiak M, Cohen LB, Friedrich RW (2006) Temporal dynamics and latency patterns of receptor neuron input to the olfactory bulb. *J Neurosci* 26:1247–1259.
9. Willhite DC, et al. (2006) Viral tracing identifies distributed columnar organization in the olfactory bulb. *Proc Natl Acad Sci USA* 103:12592–12597.
10. Illig KR, Haberly LB (2003) Odor-evoked activity is spatially distributed in piriform cortex. *J Comp Neurol* 457:361–373.
11. Rennaker RL, Chen CF, Ruyle AM, Sloan AM, Wilson DA (2007) Spatial and temporal distribution of odorant-evoked activity in the piriform cortex. *J Neurosci* 27:1534–1542.
12. Stettler DD, Axel R (2009) Representations of odor in the piriform cortex. *Neuron* 63:854–864.

NEUROSCIENCE

13. Haberly LB, Price JL (1978) Association and commissural fiber systems of the olfactory cortex of the rat. *J Comp Neurol* 178:711–740.
14. Illig KR (2005) Projections from orbitofrontal cortex to anterior piriform cortex in the rat suggest a role in olfactory information processing. *J Comp Neurol* 488:224–231.
15. Majak K, Rönkkö S, Kemppainen S, Pitkänen A (2004) Projections from the amygdaloid complex to the piriform cortex: A PHA-L study in the rat. *J Comp Neurol* 476:414–428.
16. Chabaud P, Ravel N, Wilson DA, Gervais R (1999) Functional coupling in rat central olfactory pathways: A coherence analysis. *Neurosci Lett* 276:17–20.
17. Gottfried JA, Winston JS, Dolan RJ (2006) Dissociable codes of odor quality and odorant structure in human piriform cortex. *Neuron* 49:467–479.
18. Kadohisa M, Wilson DA (2006) Separate encoding of identity and similarity of complex familiar odors in piriform cortex. *Proc Natl Acad Sci USA* 103:15206–15211.
19. Litaudon P, Amat C, Bertrand B, Vigouroux M, Buonviso N (2003) Piriform cortex functional heterogeneity revealed by cellular responses to odours. *Eur J Neurosci* 17:2457–2461.
20. Ghosh S, et al. (2011) Sensory maps in the olfactory cortex defined by long-range viral tracing of single neurons. *Nature* 472:217–220.
21. Igarashi KM, et al. (2012) Parallel mitral and tufted cell pathways route distinct odor information to different targets in the olfactory cortex. *J Neurosci* 32:7970–7985.
22. Sosulski DL, Bloom ML, Cutforth T, Axel R, Datta SR (2011) Distinct representations of olfactory information in different cortical centres. *Nature* 472:213–216.
23. Franks KM, et al. (2011) Recurrent circuitry dynamically shapes the activation of piriform cortex. *Neuron* 72:49–56.
24. Yang J, et al. (2017) Quantitative analysis of axon collaterals of single pyramidal cells of the anterior piriform cortex of the guinea pig. *BMC Neurosci* 18:25.
25. Poo C, Isaacson JS (2009) Odor representations in olfactory cortex: "Sparse" coding, global inhibition, and oscillations. *Neuron* 62:850–861.
26. Roland B, Deneux T, Franks KM, Bathellier B, Fleischmann A (2017) Odor identity coding by distributed ensembles of neurons in the mouse olfactory cortex. *eLife* 6:e26337.
27. Tantirigama ML, Huang HH, Bekkers JM (2017) Spontaneous activity in the piriform cortex extends the dynamic range of cortical odor coding. *Proc Natl Acad Sci USA* 114:2407–2412.
28. Luna VM, Pettit DL (2010) Asymmetric rostro-caudal inhibition in the primary olfactory cortex. *Nat Neurosci* 13:533–535.
29. Beed P, et al. (2013) Inhibitory gradient along the dorsoventral axis in the medial entorhinal cortex. *Neuron* 79:1197–1207.
30. Boyden ES, Zhang F, Bamberg E, Nagel G, Deisseroth K (2005) Millisecond-timescale, genetically targeted optical control of neural activity. *Nat Neurosci* 8:1263–1268.
31. Large AM, Vogler NW, Mielo S, Oswald AM (2016) Balanced feedforward inhibition and dominant recurrent inhibition in olfactory cortex. *Proc Natl Acad Sci USA* 113:2276–2281.
32. Suzuki N, Bekkers JM (2010) Distinctive classes of GABAergic interneurons provide layer-specific phasic inhibition in the anterior piriform cortex. *Cereb Cortex* 20:2971–2984.
33. Suzuki N, Bekkers JM (2012) Microcircuits mediating feedforward and feedback synaptic inhibition in the piriform cortex. *J Neurosci* 32:919–931.
34. Suzuki N, Bekkers JM (2011) Two layers of synaptic processing by principal neurons in piriform cortex. *J Neurosci* 31:2156–2166.
35. Suzuki N, Bekkers JM (2010) Inhibitory neurons in the anterior piriform cortex of the mouse: Classification using molecular markers. *J Comp Neurol* 518:1670–1687.
36. Franklin K, Paxinos G (2007) *The Mouse Brain in Stereotaxic Coordinates* (Academic, New York).
37. Large AM, Kunz NA, Mielo SL, Oswald AM (2016) Inhibition by somatostatin interneurons in olfactory cortex. *Front Neural Circuits* 10:62.
38. Isaacson JS, Scanziani M (2011) How inhibition shapes cortical activity. *Neuron* 72:231–243.
39. Sheridan DC, et al. (2014) Matching of feedback inhibition with excitation ensures fidelity of information flow in the anterior piriform cortex. *Neuroscience* 275:519–530.
40. Luna VM, Schoppa NE (2008) GABAergic circuits control input-spike coupling in the piriform cortex. *J Neurosci* 28:8851–8859.
41. Stokes CC, Isaacson JS (2010) From dendrite to soma: Dynamic routing of inhibition by complementary interneuron microcircuits in olfactory cortex. *Neuron* 67:452–465.
42. Birjandian Z, Narla C, Poulter MO (2013) Gain control of γ frequency activation by a novel feed forward disinhibitory loop: Implications for normal and epileptic neural activity. *Front Neural Circuits* 7:183.
43. Poo C, Isaacson JS (2011) A major role for intracortical circuits in the strength and tuning of odor-evoked excitation in olfactory cortex. *Neuron* 72:41–48.
44. Sturgill JF, Isaacson JS (2015) Somatostatin cells regulate sensory response fidelity via subtractive inhibition in olfactory cortex. *Nat Neurosci* 18:531–535.
45. Bekkers JM, Suzuki N (2013) Neurons and circuits for odor processing in the piriform cortex. *Trends Neurosci* 36:429–438.
46. Suzuki N, Bekkers JM (2006) Neural coding by two classes of principal cells in the mouse piriform cortex. *J Neurosci* 26:11938–11947.
47. Jammal L, Whalley B, Ghosh S, Lamrecht R, Barkai E (2016) Physiological expression of olfactory discrimination rule learning balances whole-population modulation and circuit stability in the piriform cortex network. *Physiol Rep* 4:e12830.
48. Reuveni I, Saar D, Barkai E (2013) A novel whole-cell mechanism for long-term memory enhancement. *PLoS One* 8:e68131.
49. Haberly LB (2001) Parallel-distributed processing in olfactory cortex: New insights from morphological and physiological analysis of neuronal circuitry. *Chem Senses* 26:551–576.
50. Haberly LB, Bower JM (1989) Olfactory cortex: Model circuit for study of associative memory? *Trends Neurosci* 12:258–264.
51. Hasselmo ME, Wilson MA, Anderson BP, Bower JM (1990) Associative memory function in piriform (olfactory) cortex: Computational modeling and neuropharmacology. *Cold Spring Harb Symp Quant Biol* 55:599–610.
52. Wilson DA, Sullivan RM (2011) Cortical processing of odor objects. *Neuron* 72:506–519.
53. Chen SX, Kim AN, Peters AJ, Komiyama T (2015) Subtype-specific plasticity of inhibitory circuits in motor cortex during motor learning. *Nat Neurosci* 18:1109–1115.
54. Chiu CQ, et al. (2013) Compartmentalization of GABAergic inhibition by dendritic spines. *Science* 340:759–762.
55. Cichon J, Gan WB (2015) Branch-specific dendritic Ca(2+) spikes cause persistent synaptic plasticity. *Nature* 520:180–185.
56. Fu Y, Kaneko M, Tang Y, Alvarez-Buylla A, Stryker MP (2015) A cortical disinhibitory circuit for enhancing adult plasticity. *eLife* 4:e05558.
57. Fu Y, et al. (2014) A cortical circuit for gain control by behavioral state. *Cell* 156:1139–1152.
58. Lee S, Kruglikov I, Huang ZJ, Fishell G, Rudy B (2013) A disinhibitory circuit mediates motor integration in the somatosensory cortex. *Nat Neurosci* 16:1662–1670.
59. Letzkus JJ, et al. (2011) A disinhibitory microcircuit for associative fear learning in the auditory cortex. *Nature* 480:331–335.
60. Muñoz W, Tremblay R, Levenstein D, Rudy B (2017) Layer-specific modulation of neocortical dendritic inhibition during active wakefulness. *Science* 355:954–959.
61. Pfeffer CK, Xue M, He M, Huang ZJ, Scanziani M (2013) Inhibition of inhibition in visual cortex: The logic of connections between molecularly distinct interneurons. *Nat Neurosci* 16:1068–1076.
62. Pi HJ, et al. (2013) Cortical interneurons that specialize in disinhibitory control. *Nature* 503:521–524.
63. Xu H, Jeong HY, Tremblay R, Rudy B (2013) Neocortical somatostatin-expressing GABAergic interneurons disinhibit the thalamorecipient layer 4. *Neuron* 77:155–167.
64. Chen N, Sugihara H, Sur M (2015) An acetylcholine-activated microcircuit drives temporal dynamics of cortical activity. *Nat Neurosci* 18:892–902.
65. Kuchibhotla KV, et al. (2017) Parallel processing by cortical inhibition enables context-dependent behavior. *Nat Neurosci* 20:62–71.
66. Pakan JM, et al. (2016) Behavioral-state modulation of inhibition is context-dependent and cell type specific in mouse visual cortex. *eLife* 5:e14985.
67. Padmanabhan K, et al. (2016) Diverse representations of olfactory information in centrifugal feedback projections. *J Neurosci* 36:7535–7545.
68. Chen CF, et al. (2014) Nonsensory target-dependent organization of piriform cortex. *Proc Natl Acad Sci USA* 111:16931–16936.
69. Haberly LB, Price JL (1978) Association and commissural fiber systems of the olfactory cortex of the rat. II. Systems originating in the olfactory peduncle. *J Comp Neurol* 181:781–807.
70. Datiche F, Cattarelli M (1996) Reciprocal and topographic connections between the piriform and prefrontal cortices in the rat: A tracing study using the B subunit of the cholera toxin. *Brain Res Bull* 41:391–398.
71. Piredda S, Gale K (1985) A crucial epileptogenic site in the deep prepiriform cortex. *Nature* 317:623–625.
72. Vaughan DN, Jackson GD (2014) The piriform cortex and human focal epilepsy. *Front Neurol* 5:259.
73. Zhao S, et al. (2011) Cell type–specific channelrhodopsin-2 transgenic mice for optogenetic dissection of neural circuitry function. *Nat Methods* 8:745–752.
74. Guenthner CJ, Miyamichi K, Yang HH, Heller HC, Luo L (2013) Permanent genetic access to transiently active neurons via TRAP: Targeted recombination in active populations. *Neuron* 78:773–784.
75. Clements JD, Bekkers JM (1997) Detection of spontaneous synaptic events with an optimally scaled template. *Biophys J* 73:220–229.